8-2012

Estimating the In-Plane Young's Modulus of Polycrystalline Films in MEMS

Patrick R. Cantwell
Purdue University, prcantwe@purdue.edu

Hojin Kim
Purdue University, kim0@purdue.edu

Matthew M. Schneider
Purdue University, mmschnei@purdue.edu

Hao-Han Hsu
Purdue University, hsuh@purdue.edu

Dimitrios Peroulis
Purdue University, dperouli@purdue.edu

See next page for additional authors

Cantwell, Patrick R.; Kim, Hojin; Schneider, Matthew M.; Hsu, Hao-Han; Peroulis, Dimitrios; Stach, Eric A.; and Strachan, Alejandro, "Estimating the In-Plane Young's Modulus of Polycrystalline Films in MEMS" (2012). *Birck and NCN Publications.* Paper 877.
http://dx.doi.org/10.1109/JMEMS.2012.2191939

Authors
Patrick R. Cantwell, Hojin Kim, Matthew M. Schneider, Hao-Han Hsu, Dimitrios Peroulis, Eric A. Stach, and Alejandro Strachan

Estimating the In-Plane Young's Modulus of Polycrystalline Films in MEMS

Patrick R. Cantwell, Hojin Kim, Matthew M. Schneider, Hao-Han Hsu, Dimitrios Peroulis, *Member, IEEE*, Eric A. Stach, and Alejandro Strachan

***Abstract*—Polycrystalline films in microelectromechanical systems (MEMS) sometimes have a crystallographic fiber texture that causes their in-plane Young's modulus to differ from the bulk isotropic value, which influences device behavior, lifetime, and reliability. We estimate the in-plane Young's modulus of electrodeposited nickel bridges in radio-frequency MEMS devices by measuring the crystallographic texture using X-ray diffraction and then computing a texture-weighted average of the single-crystal elastic coefficients. The nickel bridges have a 001 fiber texture and are predicted to have an in-plane Young's modulus of 195–200 GPa, about 5–7% less than the bulk isotropic value of 210 GPa. The method presented here takes into account the full distribution of crystallite orientations to predict the in-plane Young's modulus. The method is rapid, general, and capable of estimating the in-plane Young's modulus of polycrystalline film components in individual MEMS devices in an array, making it ideal for MEMS design, analysis, and quality control. [2011-0326]**

***Index Terms*—Crystallographic texture, density functional theory (DFT), elastic anisotropy, fiber texture, Hill, MAUD, molecular dynamics (MD), MTEX, preferred orientation, Reuss, single-crystal elastic tensor, Voigt, Young's modulus.**

I. Introduction

THE IN-PLANE Young's modulus of polycrystalline films used in microelectromechanical systems (MEMS) devices can deviate from the bulk isotropic value due to a preferred crystallographic orientation of the crystallites in the film [1], often referred to as *crystallographic texture*. Accurate knowledge of the in-plane Young's modulus is critical for MEMS design and analysis because it frequently plays an important role in the lifetime, reliability, and failure mechanisms of MEMS devices. For example, in the capacitive radio-frequency (RF) MEMS switches under study in this paper, the in-plane Young's modulus is related to the spring constant of the bridge and hence to the pull-down voltage required to activate the switch. Larger pull-down voltages markedly accelerate the charging of the electrode's dielectric coating [2], a key failure mechanism. An accurate estimate of the true Young's modulus is therefore critical to the design and analysis of these MEMS devices.

The Young's modulus of polycrystalline film components in MEMS can be measured directly by mechanical testing [1]. However, direct mechanical testing of microscale film structures is difficult and time consuming and has the significant disadvantage that it typically must be performed on a test film structure rather than on the film component in the MEMS device of interest.

The Young's modulus of polycrystalline films is not influenced by microscale size effects and therefore can be predicted if the crystallographic texture is known [1]. Crystallographic texture influences the Young's modulus of a polycrystalline aggregate because, in general, Young's modulus is a function of direction within a single crystallite, i.e., $E_{001} \neq E_{011} \neq E_{111}$. For example, in single-crystal nickel, $E_{001} = 130$ GPa, $E_{011} = 202$ GPa, and $E_{111} = 219$ GPa. If the crystallites in a polycrystalline film are preferentially oriented, as is frequently the case due to processes that occur during film deposition [3], the Young's modulus of the film can deviate from the bulk isotropic value, sometimes significantly.

The in-plane Young's modulus of polycrystals may be estimated by measuring their crystallographic texture using X-ray diffraction (XRD) and then calculating a texture-weighted average elastic response using the single-crystal elastic coefficients. This method is employed in this paper to predict the in-plane Young's modulus of polycrystalline electroplated nickel bridges in individual RF MEMS switches. X-ray microdiffraction optics are used to isolate individual MEMS devices for analysis, and a 2-D X-ray detector is used for rapid data acquisition, which only requires 6 min/MEMS device, approximately an order of magnitude faster than traditional pole figure texture measurements.

Previous studies have measured fiber texture in polycrystalline silicon [4] and nickel films [5]–[7] for MEMS applications using XRD [4], [6], [7] or orientation image mapping in the scanning electron microscope (SEM) [5] and estimated

Manuscript received November 4, 2011; revised March 12, 2012; accepted March 15, 2012. Date of publication April 12, 2012; date of current version July 27, 2012. This work was supported in part by the National Nuclear Security Administration Center for the Prediction of Reliability, Integrity, and Survivability of Microsystems and in part by the Department of Energy under Award DE-FC52-08NA28617. Subject Editor S. M. Spearing.

P. R. Cantwell was with the School of Materials Engineering and the Birck Nanotechnology Center, Purdue University, West Lafayette, IN 47907 USA. He is now with the Lehigh University, Bethelehem, PA 18015 USA (e-mail: prcantwell@lehigh.edu).

H. Kim and A. Strachan are with the School of Materials Engineering and the Birck Nanotechnology Center, Purdue University, West Lafayette, IN 47907 USA.

M. M. Schneider was with the School of Materials Engineering and the Birck Nanotechnology Center, Purdue University, West Lafayette, IN 47907 USA. He is now with the University of Virginia, Charlottesville, VA 22904 USA.

H.-H. Hsu was with the School of Electrical and Computer Engineering and the Birck Nanotechnology Center, Purdue University, West Lafayette, IN 47907 USA. He is now with the Intel Corporation, Hillsboro, OR 97124 USA.

D. Peroulis is with the School of Electrical and Computer Engineering and the Birck Nanotechnology Center, Purdue University, West Lafayette, IN 47907 USA.

E. A. Stach was with the School of Materials Engineering and the Birck Nanotechnology Center, Purdue University, West Lafayette, IN 47907 USA. He is now with the Electron Microscopy Group, Center for Functional Nanomaterials, Brookhaven National Laboratory, Upton, NY 11973-5000 USA.

Digital Object Identifier 10.1109/JMEMS.2012.2191939

the in-plane Young's modulus based on the results. However, these estimates of in-plane Young's modulus are based on the assumption of *perfect* fiber texture in which all crystallites are assumed to have the same orientation relative to the film normal direction. For example, for an "001 fiber texture," the calculation of in-plane Young's modulus was based on the assumption that all crystallites in the polycrystalline film were oriented such that their $\{001\}$ planes were parallel to the film surface. In contrast, the method presented here does not assume a perfect fiber texture but rather calculates the in-plane Young's modulus based on the measured distribution of crystallite orientations in the polycrystalline film thereby generating more precise predictions of the in-plane Young's modulus.

To calculate the Young's modulus based on the crystallographic texture, the single-crystal elastic coefficients of the material under study must be known. Experimentally determined values of these coefficients are available in the literature for many materials commonly used in MEMS such as Ni, Au, Al, and Si [8], [9]. However, the single-crystal elastic coefficients of many other materials of interest for MEMS applications—for example, various compositions of magnetic ternary alloys of Co, Fe, and Ni [10]—are not widely available and, in some cases, are unknown. For these materials, the elastic coefficients can be estimated with first-principle computer simulations using density functional theory (DFT) and molecular dynamics (MD).

Rapid quantification and prediction of the in-plane Young's modulus of polycrystalline film components in individual MEMS devices using the method demonstrated here are useful in many ways, such as providing more accurate information to aid in MEMS design; as a method of quality control for assessing property variations from device to device, wafer to wafer, and batch to batch; and as a way to assist in separating the effects of Young's modulus and residual stress on the mechanical behavior of MEMS components.

II. RF MEMS Switch Fabrication

The capacitive RF MEMS switches were fabricated using standard photolithograpy techniques on a thermally oxidized silicon wafer as described in [11]. The switches are composed of gold electrodes and a nickel bridge suspended over the electrodes that is anchored by four legs. The nickel bridge was fabricated by sputtering a 50-nm seed layer of titanium onto photoresist followed by a 30-nm layer of e-beam-deposited nickel. The remainder of the nickel bridge was then deposited by electroplating with a nickel sulfamate bath. The thickness of the polycrystalline nickel bridge is about 2.8 μm. The plating current density was 6 mA/cm^2, the plating temperature was 50 °C, and the bath pH was 4. A SEM image of an RF MEMS switch is shown in Fig. 1(a).

III. Microstructure Characterization

The microstructure of the nickel bridge was investigated using an FEI Tecnai T20 transmission electron microscope (TEM) operating at 200 kV. A cross-sectional TEM sample was prepared using the *in situ* lift-out method with an FEI Nova 200 NanoLab DualBeam focused ion beam/SEM.

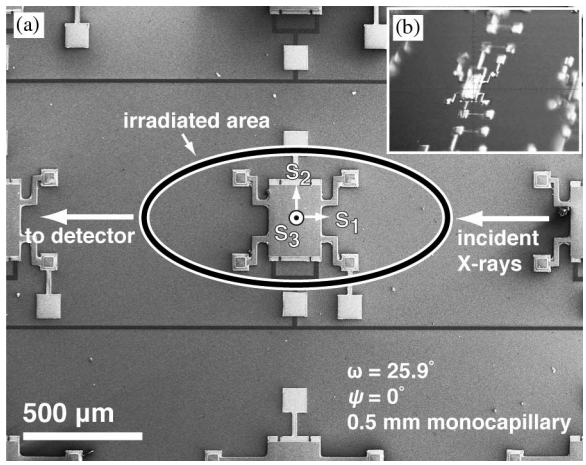

Fig. 1. Surface area irradiated by the incident X-ray beam at $\omega = 25.9°$ and $\psi = 0°$ is shown in (a) by the black oval. Inset (b) shows the alignment of the X-ray beam on an individual RF MEMS switch with a laser and video camera alignment system.

TEM bright field (BF) and dark field (DF) micrographs in Fig. 2(a) and (b) show that the polycrystalline nickel bridge is fine grained, with in-plane grain sizes on the order of 10–50 nm. The selected area electron diffraction pattern (SAEDP) in Fig. 2(c) suggests that there are two types of crystallographic fiber texture present: 001 and 111, i.e., a large volume fraction of crystallites have an orientation such that their $\{001\}$ and $\{111\}$ crystallographic planes are perpendicular to the film normal direction. Plan-view TEM images and SAEDPs (not shown) demonstrate that the in-plane grain shape is approximately equiaxed for most crystallites and that there is no in-plane preferred crystallographic texture. Hence, the texture can be described as a fiber texture, i.e., a texture with uniaxial axis of sample symmetry, which, in this case, is parallel to the film normal direction.

IV. Crystallographic Texture

A. Overview

The crystallographic texture of a MEMS polycrystalline film component must be quantified in order to predict its in-plane Young's modulus. Quantitative texture data are typically reported in terms of the orientation distribution function (ODF) $f(\mathbf{g})$ which describes the volume fraction of crystallites in the sample with a given crystallographic orientation with respect to the sample coordinate axes [12]

$$\frac{\Delta V}{V} = \frac{\int_{\Delta\Omega} f(\mathbf{g}) d\mathbf{g}}{\int_{\Omega_0} f(\mathbf{g}) d\mathbf{g}} \tag{1}$$

where V is the total volume of material, ΔV is the fraction of material with the orientation $\mathbf{g}$, Ω_0 is the full range of orientation space $(8\pi^2)$, and $\Delta\Omega$ is the range of orientation space in which ΔV resides. A common method of describing the orientation $\mathbf{g}$ is to use the Bunge convention Euler angles ϕ_1, Φ, and ϕ_2 [12], where, in general, $0 \leq \phi_1 \leq 2\pi$, $0 \leq \Phi \leq \pi$, and $0 \leq \phi_2 \leq 2\pi$. The three Euler angles describe the

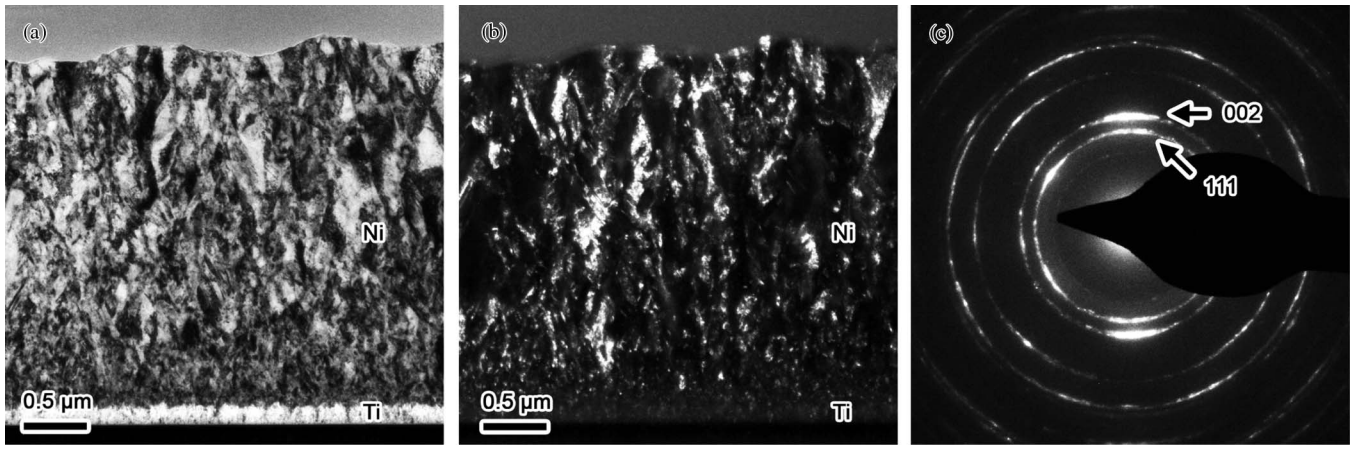

Fig. 2. Cross-sectional TEM images of a nickel bridge. (a) BF image and (b) DF image. A cross-sectional SAEDP of the nickel bridge is shown in (c) with the 111 and 002 reflections indicated.

relative orientation between sample coordinate axes and the crystallographic axes [12].

The method used in this paper to determine the ODF employs 2-D XRD measurements [13]–[15] and Rietveld refinement texture analysis. With this method, the XRD data collection time per device is only 6 min, and the texture quantification can be accomplished in about the same amount of time using the Rietveld refinement software MAUD [16].

Traditional pole figure texture measurements [12], one of the most common methods of quantifying texture, are not well suited to measuring individual microscale samples in an array because the sample must be rotated during pole figure acquisition, and it can be challenging to maintain proper alignment of the X-ray beam with a microscale sample. Pole figure measurements for texture quantification have the additional disadvantage that they can take up to several hours to complete.

The common "diffraction peak ratio" XRD technique, which employs a standard $\theta-2\theta$ powder diffractometer and is based on comparing diffraction peak heights or integrated intensities, should not be used to measure crystallographic texture. It has been shown that the peak ratio method cannot provide true quantitative texture data [17], [18] and under some circumstances will indicate an incorrect fiber texture [18].

B. Experimental Details of XRD Texture Measurement

Texture measurements using 2-D XRD [13]–[15] were carried out on a laboratory Bruker General Area Detector Diffraction System diffractometer equipped with a Hi-Star multiwire proportional counter area detector, a two-position chi stage, Cu K_α radiation, and a 0.5-mm monocapillary for microdiffraction. The monocapillary incident optics produce an incident X-ray beam with a diameter small enough to irradiate a single RF MEMS switch, thereby allowing texture quantification of polycrystalline components in individual MEMS switches as shown in Fig. 1(a). The alignment of the X-ray beam with each MEMS switch was done using a video-laser alignment system as shown in Fig. 1(b).

In 2-D XRD, diffraction data from large portions of the XRD cones can be captured simultaneously using the position-sensitive detector and then numerically integrated to provide data analogous to standard 1-D XRD data [13]. The 15 1-D XRD line profiles in Fig. 3(a) were obtained by integrating the two 2-D XRD images in Fig. 3(b). The total data collection time for the two 2-D XRD images and, hence, for the 15 1-D profiles was 6 min.

Quantitative texture analyses were carried out using the Rietveld refinement software MAUD [16]. Recalculated pole figures were exported from MAUD for further calculations and plotting with MTEX [19], [20], a MATLAB toolbox for texture analysis.

Two of the gold diffraction peaks (Au_{002} and Au_{113}) from the gold contacts of the RF MEMS switches overlap two of the nickel diffraction peaks from the bridge (Ni_{111} and Ni_{022}) as shown in Fig. 3(a). Rietveld refinement in MAUD was used to separate the contributions of Ni and Au to the intensity of these overlapping diffraction peaks so that the texture of the nickel could be quantified. A fiber texture assumption was employed during Rietveld texture analysis based on the plan-view TEM SAEDP (not shown) which indicated no preferred in-plane crystallographic orientation. The spherical harmonics model with $L = 12$ was applied.

Following the definition of penetration depth by Cullity [21], a calculation was made to estimate the penetration depth of the X-rays into the nickel film. The penetration depth is on the order of several micrometers and varies with the angles of incidence and exit. For a bulk nickel specimen, with Cu K_α radiation and equal angles of incidence and exit of 25.9°, the calculation shows that 50% of the diffracted intensity would arise from the uppermost 3.5 μm layer of nickel, while 95% of the diffracted intensity would arise from the uppermost 15.0 μm layer of nickel. These calculations show that diffraction data are collected from the entire thickness, i.e., the 2.8-μm-thick nickel films. Furthermore, the calculations are consistent with the experimental data, in which Au diffraction peaks are visible in the XRD patterns in Fig. 3. These Au diffraction peaks arise from the Au electrodes directly below the 2.8-μm-thick nickel bridge, indicating that X-rays penetrate the nickel sufficiently to provide diffraction information from the entire Ni film as well as the Au electrodes. Nevertheless, as the calculations demonstrate, the XRD data are weighted toward the top of the

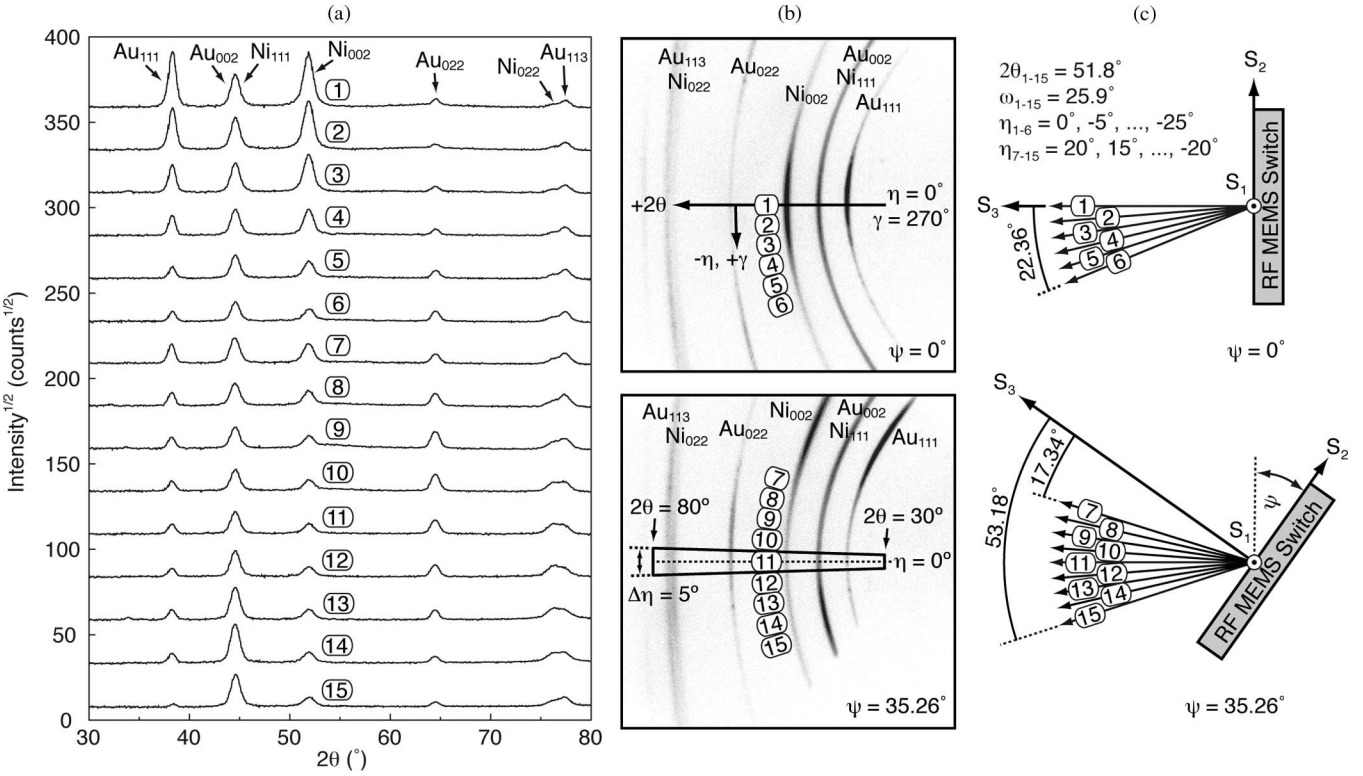

Fig. 3. Relationship between (a) the 15 1-D diffraction profiles used for texture quantification, (b) the 2-D data from which the 1-D profiles were obtained via integration, and (c) the orientation of the sample and the diffraction vectors projected into the S_2-S_3 sample coordinate plane for the Ni_{002} reflections 1–15 whose position is indicated in (a) and (b) for reference.

nickel film. This weighting will have an effect on the texture measurement and, hence, on the calculated modulus if the top of the film has a different texture than the bottom of the film, although this effect is not likely to be severe except in cases of extreme texture gradients (e.g., [22]) or if the film is thick relative to the X-ray penetration depth.

For each RF MEMS switch, two 2-D XRD images were obtained: one at $\psi = 0^\circ$ and one at $\psi = 35.26^\circ$, as shown in Fig. 3(b). These two ψ angles represent the two χ_g positions of the two-position chi stage ($\chi_g = 90^\circ - \psi$). The other two goniometer angles were held constant at $\omega = 25.9^\circ$ and $\phi = 0^\circ$. The sample-to-detector distance was $\mathbf{D} = 6$ cm, and the swing angle of the area detector, i.e., the angle between the center of the detector and the incident X-ray beam, was held constant at $\alpha = 51.8^\circ$. The notation conventions used here follow [13].

An inverse pole figure for the sample normal direction is shown in Fig. 4. Two fiber textures are present: a strong 001 fiber texture and a weak 111 fiber texture, consistent with the cross-sectional TEM SAEDP in Fig. 2. The Rietveld refinement software MAUD provides three "goodness-of-fit" parameters that quantify the agreement between the experimental data and the refined model. For the inverse pole figure shown in Fig. 4, $R_w = 23.34\%$, $R_{\text{exp}} = 16.15\%$, and $\sigma = 1.45$, where $\sigma = R_w/R_{\text{exp}}$. A good fit is indicated by $1 \leq \sigma \leq 2$. To further ensure that the texture analysis has been successful, it is useful to compare the texture model against the experimental data, which is done within the MAUD software [16], and also to check that the calculated texture results are consistent with the original 2-D XRD patterns.

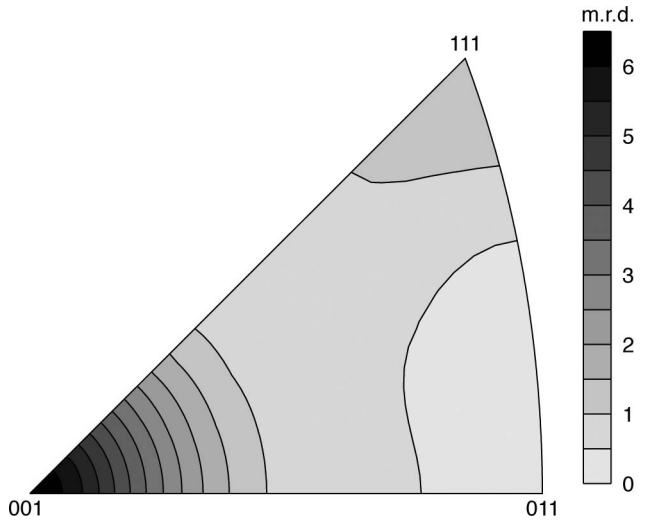

Fig. 4. Inverse pole figure (normal direction) showing the crystallographic texture of the polycrystalline nickel bridge in an RF MEMS switch (contour lines every 0.5 m.r.d.). There are two fiber texture components: a relatively strong fiber texture component of (001) with maximum m.r.d. of about 6.4 and a weak secondary (111) fiber texture component with m.r.d. between 1 and 1.5.

V. Calculating the In-Plane Young's Modulus

A. Overview

After obtaining the ODF from XRD measurements, a texture-weighted average of the nickel single-crystal elastic coefficients must be calculated to predict the in-plane Young's modulus of the polycrystalline film components in each MEMS device.

This was done using the classic Voigt [23], Reuss [24], and Hill [25] polycrystal elastic averages. The Voigt and Reuss averages assume constant strain and constant stress in the crystallites, respectively, and provide upper and lower bounds on the elastic properties, respectively. The Hill average [25] is an arithmetic mean of the Voigt and Reuss averages.

Although the Hill average lacks a fundamental theoretical justification, it has been shown to agree reasonably well with experiment for materials with low-to-moderate single-crystal anisotropy [26], [27]. Thus, the Hill average will be primarily employed here for making predictions of in-plane Young's modulus, and the Voigt and Reuss averages will be reported where appropriate to provide estimates of lower and upper bounds on the predictions.

All three averages (Reuss, Voigt, and Hill) were calculated using built-in functions in MTEX [19], [20]. The MTEX software makes the computation of the Voigt, Reuss, and Hill averages and Young's modulus straightforward and routine.

The volume fraction ΔV of material at each orientation $\mathbf{g}$ in $f(\mathbf{g})$ is normalized so that a uniform orientation distribution (i.e., no preferred crystallographic orientation or texture) has the value $f(\mathbf{g}) = 1$ for all orientations. These normalized units are called "multiples of a random distribution" (m.r.d.). In a sample with crystallographic texture where a larger volume fraction of crystallites with a given orientation $\mathbf{g}_0$ exist than in a nontextured sample, $f(\mathbf{g}_0)$ has an m.r.d. greater than one. If the opposite is true, then the m.r.d. is less than one.

Even though the full orientation space is $8\pi^2$, symmetry can reduce the amount of orientation space required to describe all orientations for a given crystal. The smallest region of orientation space that meets this requirement is called the *fundamental zone* [12]. For cubic crystals, the fundamental zone can be represented by a triangular region of a standard stereographic projection that occupies 1/24th of the full orientation space. This standard stereographic triangle, whose corners are (001), (011), and (111), is often used to represent inverse pole figures in the cubic crystal system, for example, as shown in Fig. 4.

The only inputs required by the MTEX software to calculate the Reuss, Voigt, and Hill averages and the in-plane Young's modulus are the following: 1) the recalculated pole figures exported from MAUD and 2) the single-crystal elastic coefficients for nickel, which were obtained from experimentally determined published values [8]. The theory and mathematics behind the calculations are summarized in this section.

B. Single-Crystal Elastic Coefficients

The single-crystal elastic coefficients are fourth-rank property tensors [28] and include the stiffness coefficient tensor C_{ijkl} and the compliance coefficient tensor S_{ijkl}. Due to a high degree of symmetry, cubic crystals such as nickel have only three independent elastic coefficients, i.e., C_{11}, C_{12}, and C_{44} and S_{11}, S_{12}, and S_{44}.

Young's modulus relates strain to stress through Hooke's law

$$\sigma = E\epsilon. \tag{2}$$

In single crystals, the elastic properties are not isotropic, i.e., they are a function of direction within the crystal, and a tensor property description is employed [28]. Similar to the isotropic case, Hooke's law for the anisotropic case of single crystals uses the stiffness tensor C_{ijkl} to relate the strain tensor to the stress tensor

$$\sigma_{ij} = C_{ijkl}\epsilon_{kl}, \qquad i,j,k,l = 1,2,3. \tag{3}$$

The single-crystal compliance tensor S_{ijkl} gives the inverse relationship

$$\epsilon_{ij} = S_{ijkl}\sigma_{kl}, \qquad i,j,k,l = 1,2,3 \tag{4}$$

where Einstein summation notation has been used [28]. Matrix notation may be used to simplify the relationships

$$\epsilon_i = S_{ij}\sigma_j, \qquad i,j = 1,2,\ldots,6 \tag{5}$$

$$\sigma_i = C_{ij}\epsilon_j, \qquad i,j = 1,2,\ldots,6. \tag{6}$$

The equation that relates strain to stress using the three independent stiffness coefficients C_{11}, C_{12}, and C_{44} can be written out completely as follows:

$$\begin{bmatrix}\sigma_1\\ \sigma_2\\ \sigma_3\\ \sigma_4\\ \sigma_5\\ \sigma_6\end{bmatrix} = \begin{bmatrix}C_{11} & C_{12} & C_{12} & 0 & 0 & 0\\ C_{12} & C_{11} & C_{12} & 0 & 0 & 0\\ C_{12} & C_{12} & C_{11} & 0 & 0 & 0\\ 0 & 0 & 0 & C_{44} & 0 & 0\\ 0 & 0 & 0 & 0 & C_{44} & 0\\ 0 & 0 & 0 & 0 & 0 & C_{44}\end{bmatrix}\begin{bmatrix}\epsilon_1\\ \epsilon_2\\ \epsilon_3\\ \epsilon_4\\ \epsilon_5\\ \epsilon_6\end{bmatrix}. \tag{7}$$

C. Reuss, Voigt, and Hill Polycrystal Elastic Averages

If the ODF $f(\mathbf{g})$ and the single-crystal elastic coefficients are known, the average elastic properties of the sample can be determined by averaging the elastic coefficients over the ODF. There is not a unique method of obtaining such a polycrystal elasticity average, and several different methods exist [12]. The averages employed in this paper are the Voigt [23], Reuss [24], and Hill [25] averages. The Reuss and Voigt averages can be written as [27]

$$S^R_{ijkl} = \overline{S}_{ijkl} = \oint S_{ijkl}(\mathbf{g}) f(\mathbf{g})\, d(\mathbf{g}) \tag{8}$$

$$C^V_{ijkl} = \overline{C}_{ijkl} = \oint C_{ijkl}(\mathbf{g}) f(\mathbf{g})\, d(\mathbf{g}) \tag{9}$$

where $f(\mathbf{g})$ is the ODF, S_{ijkl} and C_{ijkl} are the elastic compliance and stiffness coefficients, respectively, of a single crystal with respect to the specimen coordinate system, and the integration is over all orientation space. Equations (8) and (9) represent an orientation-weighted average of the elastic and stiffness coefficients, which is based on the fraction of material in each orientation $\mathbf{g}$ present in the specimen. These equations allow an effective average stiffness tensor and compliance tensor to be calculated for the specimen based on its crystallographic texture, as measured by XRD, combined with its single-crystal elastic coefficients. These average tensors are then used to calculate the effective in-plane Young's modulus of the specimen.

TABLE I
REUSS, VOIGT, AND HILL AVERAGE VALUES OF IN-PLANE YOUNG'S MODULUS FOR THE NICKEL BRIDGE IN TWO BATCHES OF RF MEMS SWITCHES, CALCULATED USING EXPERIMENTAL VALUES OF SINGLE-CRYSTAL ELASTIC COEFFICIENTS FROM TABLE III. THE IN-PLANE YOUNG'S MODULI OF A SIMULATED PERFECT 001 FIBER TEXTURE SAMPLE AND A UNIFORM TEXTURE SAMPLE ARE ALSO GIVEN

	Perfect 001 Texture (GPa)	RF MEMS Switches (batch #1) (GPa)	RF MEMS Switches (batch #2) (GPa)	Uniform Texture (GPa)
$E_{in-plane}^{Reuss}$	163.3	178.8 ± 1.1	183.3 ± 1.0	192.4
$E_{in-plane}^{Hill}$	172.4	194.7 ± 1.3	199.9 ± 1.1	209.7
$E_{in-plane}^{Voigt}$	182.7	210.3 ± 1.5	216.1 ± 1.2	225.7

The Hill average [25], an arithmetic mean of the Voigt and Reuss averages, can be written as [27]

$$S_{ijkl}^{\text{Hill}} = \frac{1}{2}\left(S_{ijkl}^{R} + S_{ijkl}^{V}\right) \tag{10}$$

where $S_{ijkl}^{V} = (C_{ijkl}^{V})^{-1}$. The in-plane Young's modulus (Voigt, Reuss, or Hill average) can then be computed by taking the inverse of the appropriate compliance tensor coefficient S_{11} or S_{22}. For example, to calculate the in-plane Young's modulus based on the Hill average elastic behavior, the equation is

$$E_{\text{in-plane}}^{\text{Hill}} = \frac{1}{S_{11}^{\text{Hill}}} = \frac{1}{S_{22}^{\text{Hill}}}\left(\neq \frac{1}{S_{33}^{\text{Hill}}}\right). \tag{11}$$

The predicted values of in-plane Young's modulus for the nickel bridge of the RF MEMS switches are presented in Table I.

VI. EFFECT OF CRYSTALLOGRAPHIC TEXTURE ON IN-PLANE YOUNG'S MODULUS OF NICKEL AND OTHER MATERIALS FOR MEMS APPLICATIONS

The method presented thus far is sufficient to predict the in-plane Young's modulus of polycrystalline film components in individual MEMS devices using XRD texture measurements if the single-crystal elastic coefficients of the material are known. The value of applying the method depends on how accurately the in-plane Young's modulus must be known for a given application and on the range of possible in-plane Young's moduli for a given material, which is related to the degree of single-crystal elastic anisotropy of the material. In this section, calculations are made to show the range of in-plane Young's moduli that can be expected for various types and strengths of crystallographic fiber textures in nickel and other materials of interest for MEMS applications such as polycrystalline silicon, aluminum, and gold.

A. Fiber Texture Elastic Anisotropy

A key metric for understanding the potential influence of crystallographic texture on in-plane Young's modulus is the *anisotropy factor* A [12]. The anisotropy factor for cubic crystals is defined by the three independent single-crystal elastic coefficients as follows [29]:

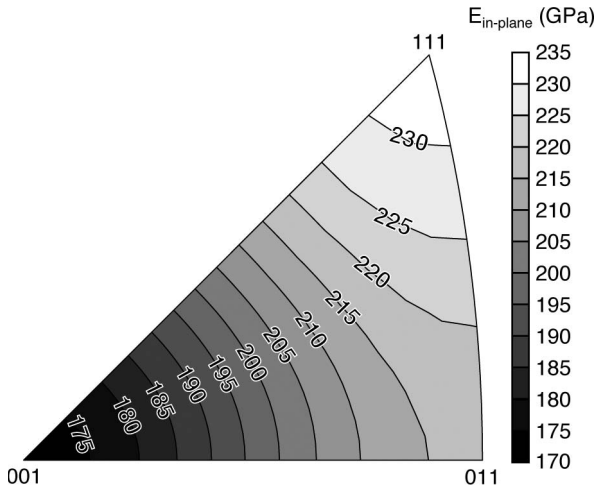

Fig. 5. Stereogram showing the calculated Hill average in-plane Young's modulus $E_{\text{in-plane}}^{\text{Hill}}$ for the the full range of possible *perfect* single fiber textures in nickel films. The in-plane Young's modulus ranges from 172 GPa for a film with perfect 001 fiber texture to 232 GPa for a film with perfect 111 fiber texture.

$$A = \frac{C_{44}}{\frac{1}{2}(C_{11} - C_{12})} = \frac{2(S_{11} - S_{12})}{S_{44}}. \tag{12}$$

If $A = 1$, the material is elastically isotropic, and its behavior can be described by two independent elastic constants rather than three. Nickel is markedly anisotropic with $A = 2.43$, which suggests that crystallographic texture can significantly influence the in-plane Young's modulus of nickel.

To demonstrate the influence of various types of crystallographic fiber texture on the in-plane Young's modulus of nickel, the Hill average in-plane Young's modulus was calculated for each possible type of *perfect* fiber texture in nickel. The minimum and maximum Hill average in-plane Young's moduli are 172 and 232 GPa for perfect 001 and 111 fiber textures, respectively. Thus, the Hill average predicts that a nickel film with any other fiber texture will have an in-plane Young's modulus that falls within the range 172 GPa $\leq E_{\text{in-plane}} \leq$ 232 GPa, as shown in the contour plot in Fig. 5. The Hill average has been shown to agree well with experimental values of polycrystalline elastic modulus for moderate values of single-crystal anisotropy [26] and, therefore, proves practically useful in many cases even though it is simply a geometric average. The maximum in-plane Young's modulus predicted by the Hill average is 1.35 times larger than the minimum in-plane Young's modulus. We call this value the *fiber texture elastic anisotropy factor* F where

$$F = \frac{E_{\text{in-plane}}^{\max}}{E_{\text{in-plane}}^{\min}}. \tag{13}$$

Experimentally measured values of Young's moduli for nickel films that lie within the range 172 GPa $\leq E_{\text{in-plane}} \leq$ 232 GPa can potentially be explained by crystallographic fiber

TABLE II
EFFECT OF CRYSTALLOGRAPHIC TEXTURE ON IN-PLANE YOUNG'S MODULUS IN POLYCRYSTALLINE ALUMINUM, SILICON, NICKEL, AND GOLD. THESE MATERIALS ARE COMMON IN MEMS AND HAVE FCC AND FCC-RELATED CRYSTAL STRUCTURES. THE ANISOTROPY FACTOR A, THE HILL AVERAGE IN-PLANE YOUNG'S MODULUS FOR PERFECT FIBER TEXTURES 001, 011, AND 111, AND THE FIBER TEXTURE ELASTIC ANISOTROPY F ARE GIVEN FOR EACH MATERIAL

Material	A	$E^{001}_{in-plane}$ (GPa)	$E^{011}_{in-plane}$ (GPa)	$E^{111}_{in-plane}$ (GPa)	F
Al	1.22	67.7	71.1	72.3	1.07
Si	1.56	149	166	172	1.15
Ni	2.43	172	216	232	1.35
Au	2.85	59.9	80.3	87.9	1.47

texture. If measurements indicate a value for Young's modulus that lies significantly outside this range, then other explanations should be sought, for example, experimental error or sample porosity.

The fiber texture elastic anisotropy factor F and Hill average values of in-plane Young's modulus for 001, 011, and 111 perfect fiber textures were calculated for several materials of interest for MEMS applications, including polycrystalline silicon, aluminum, and gold, based on elastic coefficients in [9]. The in-plane Young's moduli for these materials follows the same trend shown in Fig. 5 for nickel. The results, shown in Table II, demonstrate that larger values of A are correlated with larger values of F. The larger the value of F, the greater the influence of crystallographic texture on in-plane Young's modulus, and thus, the more important it becomes to estimate the Young's modulus based on texture measurements using the method demonstrated in this paper.

B. Real Films With Fiber Texture

The range of in-plane Young's modulus for real fiber-textured polycrystalline films will be somewhat smaller than the range shown in Fig. 5 and Table II because real films rarely, if ever, have perfect or near-perfect fiber texture. More often, their fiber texture has a finite angular spread or mosaicity, such that other orientations exist in addition to those whose hkl poles are perfectly parallel to the film normal direction.

Calculations were made to illustrate how the in-plane Young's modulus evolves with increasing degree of fiber texture in nickel, from near-uniform texture (i.e., a nontextured sample) to near-perfect fiber texture. The calculations were made by modeling the three fiber textures 001, 011, and 111 in MTEX [19], [20] and calculating their Hill average in-plane Young's modulus as a function of decreasing fiber texture halfwidth, i.e., increasing strength or degree of fiber texture. The results are shown in Fig. 6 and demonstrate that weak 001, 011, and 111 fiber textures all have in-plane Young's moduli similar to the bulk isotropic value. As each texture becomes stronger, the in-plane Young's modulus deviates more and more from the bulk isotropic value. The 001 fiber texture has the effect of reducing the in-plane Young's modulus, while the 011 and 111 fiber textures increase the in-plane Young's modulus.

These calculations show that the in-plane Young's modulus of a polycrystalline film component in a MEMS device depends upon the elastic anisotropy of the material from which it is made and the type and strength or degree of crystallographic fiber texture.

VII. COMPUTER SIMULATIONS TO PREDICT ELASTIC COEFFICIENTS

Experimental values of single-crystal elastic coefficients are sometimes not available in the literature for a material of interest. In such instances, it is possible to predict the elastic coefficients using computer simulations. As an example, we use DFT and MD to predict the elastic coefficients of nickel.

The DFT simulations were performed using SeqQuest, an electronic structure code from Sandia National Laboratories [30], which is available for online simulation at nanoHUB.org [31]. The MD simulations were performed using a Large-scale Atomic/Molecular Massively Parallel Simulator [32]. In both cases, two different volume-conserving deformations and an isotropic expansion were applied to the material, and variation in system energy (for zero temperature) or stress (at finite temperatures) with incremental applied strain was used to obtain three independent elastic constants. Volume-conserving tetragonal and orthorhombic deformations were used to obtain the shear moduli C_{44} and C', where $C' = 1/2(C_{11} - C_{12})$. A deformation of pure dilation was performed to determine the bulk modulus B where $B = 1/3(C_{11} + 2C_{12})$. Bulk modulus is a measure of a material's volume change in response to applied uniform pressure, i.e., $B = V(\partial P/\partial V)$, where B is the bulk modulus, V is the volume, and $\partial P/\partial V$ is the partial derivative of pressure with respect to volume. After determining C' and B, the elastic constants C_{11} and C_{12} were calculated from the equations that relate C' and B to C_{11} and C_{12}.

In the DFT simulations, a spin-polarized functional with the generalized gradient approximation was employed using the Perdew–Burke–Ernzerhof implementation [33] on bulk single-crystal nickel. Simulation cells for the finite temperature MD simulations consist of $10 \times 10 \times 10$ replications of the face-centered cubic (FCC) unit cell, and an embedded atom model developed by Angelo *et al.* [34] is used to describe atomic interactions. Before deformation, the system was equilibrated at the desired temperature and ambient pressure using isothermal isobaric MD simulations. Elastic constants were calculated at a series of temperatures from $T = 50$ K to $T = 450$ K.

Elastic coefficients calculated by DFT and MD are shown in Fig. 7. The results show that the DFT predictions (with no adjustable parameters) are within 9% of the zero temperature experimental values [35]; this is the typical accuracy of this level of theory and is consistent with prior results [36]. The MD results characterize the softening of the material with temperature and show that C_{11} is more temperature dependent than C_{12} and C_{44}, in agreement with experiments [35]. The room temperature elastic constants calculated from the MD simulations are within 11% of the experimental results.

Thus, computer simulations can be used to estimate the elastic stiffness coefficients when experimental values are not available and, therefore, may prove useful in estimating the

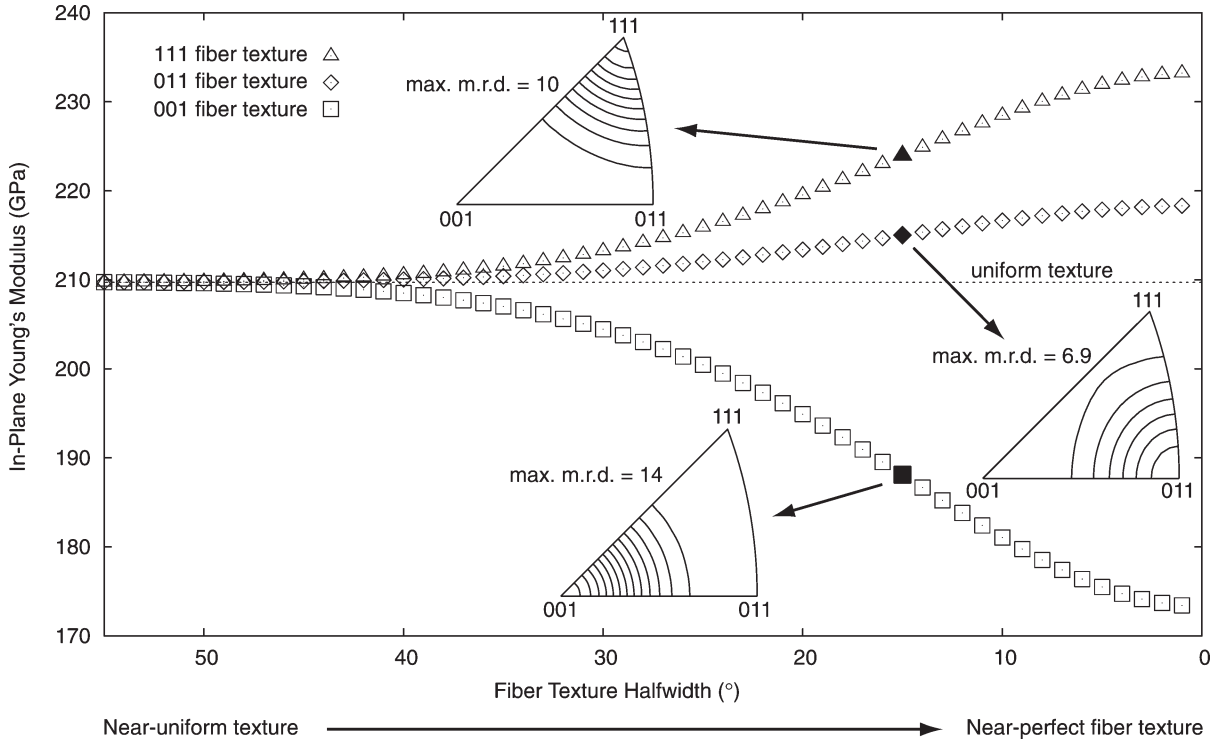

Fig. 6. Evolution of in-plane Young's modulus (Hill average) of nickel as a function of fiber texture strength for the three low-index fiber textures 001, 011, and 111, from near-uniform texture on the left to near-perfect fiber texture on the right. Inverse pole figures for the sample normal direction are shown for the three different fiber textures with fiber texture halfwidth of 15°, with contour lines plotted every 1 m.r.d.

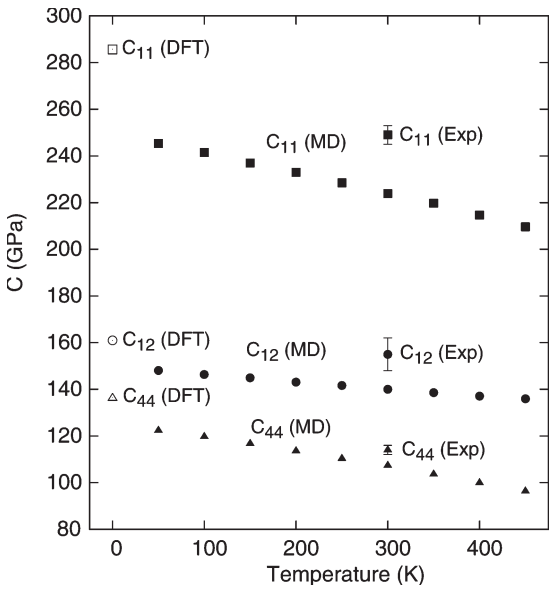

Fig. 7. Elastic stiffness coefficients C_{11}, C_{12}, and C_{44} computed by (open symbols) DFT and (closed symbols, in 50-K increments) MD simulations. For comparison, (closed symbols with error bars) experimentally derived values of the elastic stiffness coefficients from Table III are included. The DFT values give the $T = 0$ K value of the coefficients, while the MD values show how the coefficients change with temperature.

in-plane Young's modulus of thin films in MEMS in conjunction with the method demonstrated here. As illustrated by the MD results in Fig. 7, it is emphasized that elastic coefficients are not constant but do indeed vary with temperature, which may be an important consideration for MEMS devices in service at extreme temperatures.

TABLE III
SINGLE-CRYSTAL ELASTIC STIFFNESS COEFFICIENTS FOR NICKEL [8]

	C_{11} (GPa)	C_{12} (GPa)	C_{44} (GPa)
Exp.	249 ± 4	155 ± 7	114 ± 12

VIII. RESULTS AND DISCUSSION

The crystallographic texture of the polycrystalline nickel bridge in 20 RF MEMS switches—ten switches each from two separate batches—was quantified using 2-D XRD crystallographic texture measurements and the Rietveld refinement software MAUD [16] as described in Section IV. Recalculated pole figures were imported into the texture analysis software MTEX [19], [20], and the orientation-weighted polycrystal Reuss, Hill, and Voigt average elastic compliance tensors—S^R_{ijkl}, S^H_{ijkl}, and S^V_{ijkl}—were calculated. The in-plane Young's modulus for each average tensor was determined using (11). It was found that the Hill average in-plane Young's modulus of the nickel bridge was 194.7 ± 1.3 GPa for batch #1 and 199.9 ± 1.1 GPa for batch #2, as shown in Table I along with the Reuss and Voigt average values. These estimated in-plane Young's modulus values are about 5%–7% less than the bulk isotropic value of Young's modulus for nickel, which is about 210 GPa. The differences between the two batches in texture and predicted Young's modulus are due to unintended batch-to-batch variation. The plating bath and all plating parameters were nominally identical for both batches. This illustrates how the method can be useful to assess the effects of unintended batch-to-batch variation on the elastic properties and, hence, performance of MEMS devices.

This reduced in-plane Young's modulus is expected because the nickel films have a 001 fiber texture which reduces the in-plane Young's modulus as shown in Fig. 6. However, the 001 fiber texture is not a *perfect* fiber texture, and there is also a weak 111 texture present, both of which have the effect of increasing the in-plane Young's modulus relative to the expected value for a film with perfect 001 fiber texture, as shown in Fig. 6. Therefore, the in-plane Young's modulus of the nickel bridges is not 172 GPa (18% less than the isotropic Young's modulus) as would be expected for a film with perfect 001 fiber texture. Rather, the in-plane Young's modulus of the nickel bridges is predicted to be intermediate between that of a perfect 001 fiber texture (172 GPa) and that of a uniform texture (209.7 GPa) as shown in Table I. These predictions and the calculations in Section VI demonstrate the importance of taking into account the degree of fiber texture, i.e., the orientation distribution, when estimating the in-plane Young's modulus based on crystallographic texture.

IX. Conclusion

A method has been demonstrated for the prediction of in-plane Young's modulus of polycrystalline film components in individual MEMS devices by rapidly quantifying their crystallographic texture using 2-D XRD and calculating an orientation-weighted average of the single-crystal elastic coefficients. Additionally, a first-principle DFT simulation method for determining the single-crystal elastic coefficients necessary for the calculation has been presented in the event that the elastic coefficients are not available from published experimental data.

The method presented here for the quantitative prediction of in-plane Young's modulus of components in MEMS devices has several key advantages over previous methods: 1) It is based on a full quantitative texture measurement; 2) it does not assume an idealized perfect fiber texture; 3) it is capable of measuring individual MEMS devices in an array of devices if appropriate microdiffraction incident optics are used; 4) it is rapid, with data collection time on the order of 5–10 min; 5) it may be used on MEMS devices composed of multiple materials with overlapping XRD peaks; and 6) for materials whose single-crystal elastic coefficients are not available in the literature, DFT and MD computer simulations may be used to estimate coefficients.

The technique was applied to polycrystalline nickel bridges in RF MEMS switches, and the in-plane Young's modulus of the nickel bridges was predicted to be about 195–200 GPa, about 5%–7% less than the isotropic value of 210 GPa.

References

[1] K. J. Hemker and J. W. N. Sharpe, "Microscale characterization of mechanical properties," *Annu. Rev. Mater. Res.*, vol. 37, pp. 93–126, Feb. 2007.

[2] C. Goldsmith, J. Ehmke, A. Malczewski, B. Pillans, S. Eshelman, Z. Yao, J. Brank, and M. Eberly, "Lifetime characterization of capacitive RF MEMS switches," in *IEEE MTT-S Int. Microw. Symp. Dig.*, Phoenix, AZ, May 2001, vol. 1, pp. 227–230.

[3] I. Petrov, P. B. Barna, L. Hultman, and J. E. Greene, "Microstructural evolution during film growth," *J. Vac. Sci. Technol. A, Vac. Surf. Films*, vol. 21, no. 5, pp. S117–S128, Sep. 2003.

[4] S. W. Lee, C. H. Cho, J. P. Kim, S. J. Park, S. W. Yi, J. J. Kim, and D. D. Cho, "The effects of texture and doping on the Young's modulus of polysilicon," *Microelectromech. Struct. Mater. Res.*, vol. 518, pp. 21–26, 1998.

[5] K. J. Hemker and H. Last, "Microsample tensile testing of LIGA nickel for MEMS applications," *Mater. Sci. Eng. A*, vol. 319–321, pp. 882–886, Dec. 2001.

[6] T. Fritz, H. S. Cho, K. J. Hemker, W. Mokwa, and U. Schnakenberg, "Characterization of electroplated nickel," *Microsyst. Technol.*, vol. 9, no. 1/2, pp. 87–91, Nov. 2002.

[7] H. S. Cho, K. J. Hemker, K. Lian, J. Goettert, and G. Dirras, "Measured mechanical properties of LIGA Ni structures," *Sens. Actuators A, Phys.*, vol. 103, no. 1/2, pp. 59–63, Jan. 2003.

[8] H. M. Ledbetter and R. P. Reed, "Elastic properties of metals and alloys, I. Iron, nickel, and iron–nickel alloys," *J. Phys. Chem. Ref. Data*, vol. 2, no. 3, pp. 531–617, Jul. 1973.

[9] H. Ledbetter and S. Kim, *Handbook of Elastic Properties of Solids, Liquids, and Gases*. New York: Academic, 2001, ch. Monocrystal elastic constants and derived properties of the cubic and hexagonal elements, pp. 97–106.

[10] N. V. Myung, D.-Y. Park, B.-Y. Yoo, and P. T. A. Sumodjo, "Development of electroplated magnetic materials for MEMS," *J. Magn. Magn. Mater.*, vol. 265, no. 2, pp. 189–198, Sep. 2003.

[11] H.-H. Hsu and D. Peroulis, "A viscoelastic-aware experimentally-derived model for analog RF MEMS varactors," in *Proc. IEEE 23rd Int. Conf. MEMS*, Jan. 2010, pp. 783–786.

[12] U. F. Kocks, C. N. Tomé, and H.-R. Wenk, *Texture and Anisotropy: Preferred Orientations in Polycrystals and Their Effect on Materials Properties*., 1st ed. Cambridge, U.K.: Cambridge Univ. Press, 1998.

[13] B. B. He, *Two-Dimensional X-Ray Diffraction*., 1st ed. Hoboken, NJ: Wiley, Jul. 2009.

[14] B. B. He, "Introduction to two-dimensional X-ray diffraction," *Powder Diffract.*, vol. 18, no. 2, pp. 71–85, 2003.

[15] B. B. He, "Microdiffraction using two-dimensional detectors," *Powder Diffract.*, vol. 19, no. 2, pp. 110–118, 2004.

[16] L. Lutterotti, M. Bortolotti, G. Ischia, and I. Lonardelli, "Rietveld texture analysis from diffraction images," *Z. Kristallogr. Suppl.*, vol. suppl. 26, pp. 125–130, Nov. 2007.

[17] J. L. Jones, E. B. Slamovich, and K. J. Bowman, "Critical evaluation of the Lotgering degree of orientation texture indicator," *J. Mater. Res.*, vol. 19, no. 11, pp. 3414–3422, Nov. 2004.

[18] H. R. Wenk, M. Sintubin, J. Huang, G. C. Johnson, and R. T. Howe, "Texture analysis of polycrystalline silicon films," *J. Appl. Phys.*, vol. 67, no. 1, pp. 572–574, Jan. 1990.

[19] R. Hielscher and H. Schaeben, "A novel pole figure inversion method: Specification of the MTEX algorithm," *J. Appl. Crystallography*, vol. 41, no. 6, pp. 1024–1037, Dec. 2008.

[20] D. Mainprice, R. Hielscher, and H. Schaeben, "Calculating anisotropic physical properties from texture data using the MTEX open source package," in *Deformation Mechanism, Rheology & Tectonics: Microstructures, Mechanics & Anisotropy—The Martin Casey Volume*, D. Prior, E. H. Rutter, and D. J. Tatham, Eds. London, U.K.: Geological Soc. London, 2011.

[21] B. D. Cullity, *Elements of X-Ray Diffraction*. Reading, MA: Addison-Wesley, 1978.

[22] M. Birkholz, N. Darowski, and I. Zizak, "Profiling of fibre texture gradients in thin films by anomalous X-ray diffraction," *Z. Kristallogr. Suppl.*, vol. 27, pp. 263–271, 2008.

[23] W. Voigt, *Lehrbuch der Kristallphysik*. Leipzig, Germany: B.G. Teubner, 1928.

[24] A. Reuss, "Berechnung der fliessgrenze von mischkristallen auf grund der plastizitätsbedingung für einkristalle," *Z. Angew Math. Mech.*, vol. 9, no. 1, pp. 49–58, 1929.

[25] R. Hill, "The elastic behavior of a crystalline aggregate," *Proc. Phys. Soc. A*, vol. 65, no. 5, pp. 349–354, May 1952.

[26] D. H. Chung and W. R. Buessem, "The Voigt–Reuss–Hill approximation and elastic moduli of MgO, CaF2, beta-ZnS, ZnSe, and CdTe," *J. Appl. Phys.*, vol. 38, no. 6, pp. 2535–2540, May 1967.

[27] H.-J. Bunge and W. T. Roberts, "Orientation distribution, elastic and plastic anisotropy in stabilized steel sheet," *J. Appl. Crystallogr.*, vol. 2, no. 3, pp. 116–128, Aug. 1969.

[28] J. F. Nye, *Physical Properties of Crystals*, 2nd ed. New York: Oxford Science Publ., 1985.

[29] K. Bowman, *Mechanical Behavior of Materials*. Hoboken, NJ: Wiley, 2004.

[30] P. A. Schultz, SeqQuest: Density Functional Theory Code From Sandia National Laboratories. [Online]. Available: http://dft.sandia.gov/Quest

[31] R. P. K. Vedula, G. Bechtol, B. P. Haley, and A. Strachan. (2011, Mar.) "nanoMATERIALS SeqQuest DFT," (Version 1.3), DOI: 10254/nanohub-r3982.4. [Online]. Available: http://nanohub.org/resources/nmst_dft
[32] S. Plimpton, "Fast parallel algorithms for short-range molecular dynamics," *J. Comput. Phys.*, vol. 117, no. 1, pp. 1–19, Mar. 1995.
[33] J. P. Perdew, K. Burke, and M. Ernzerhof, "Generalized gradient approximation made simple," *Phys. Rev. Lett.*, vol. 77, no. 18, pp. 3865–3868, Oct. 1996.
[34] J. E. Angelo, N. R. Moody, and M. I. Baskes, "Trapping of hydrogen to lattice defects in nickel," *Modell. Simul. Mater. Sci. Eng.*, vol. 3, no. 3, pp. 289–307, May 1995.
[35] G. A. Alers, J. R. Neighbours, and H. Sato, "Temperature dependent magnetic contributions to the high field elastic constants of nickel and an Fe–Ni alloy," *J. Phys. Chem. Solids*, vol. 13, no. 1/2, pp. 40–55, May 1960.
[36] P. Söderlind, O. Eriksson, J. M. Wills, and A. M. Boring, "Theory of elastic constants of cubic transition metals and alloys," *Phys. Rev. B*, vol. 48, no. 9, pp. 5844–5851, Sep. 1993.

Patrick R. Cantwell received the A.B. degree in engineering sciences from Dartmouth College, Hanover, NH, in 2004, the B.E. and M.S. degrees in engineering sciences from Thayer School of Engineering, Dartmouth College, in 2006, and the Ph.D. degree in materials science and engineering from Purdue University, West Lafayette, IN, in 2011.

He is currently a Postdoctoral Research Associate with the Center for Advanced Materials and Nanotechnology, Lehigh University, Bethlehem, PA.

Hojin Kim received the B.S. degree from the School of Chemical Engineering and Material Science, Chung-Ang University, Seoul, Korea, and the Ph.D. degree in chemical engineering from The University of Utah, Salt Lake.

He is currently a Postdoctoral Research Associate with the School of Materials Engineering, Purdue University, West Lafayette, IN.

Matthew M. Schneider received the B.S. degree in materials science and engineering from Purdue University, West Lafayette, IN, in 2011. He is currently working toward the Ph.D. degree in materials science and engineering at the University of Virginia, Charlottesville.

He was with the Birck Nanotechnology Center at Purdue University.

Hao-Han Hsu received the B.S. and M.S. degrees in electrical engineering from National Tsing Hua University, Hsinchu, Taiwan, in 2001 and 2002, respectively, and the Ph.D. degree from the School of Electrical and Computer Engineering, Purdue University, West Lafayette, IN. His Ph.D. thesis focused on the reliability of radio-frequency microelectromechanical systems devices.

He is currently an Electromagnetic Compatibility Engineer with Intel Corporation, Hillsboro, OR.

Dr. Hsu was the recipient of the Student Paper Award at the 2011 IEEE Topical Meeting on Silicon Monolithic Integrated Circuits in RF Systems.

Dimitrios Peroulis (S'99–M'04) received the Ph.D. degree in electrical engineering from the University of Michigan, Ann Arbor, in 2003.

Since August 2003, he has been with Purdue University, West Lafayette, IN, where he is currently leading a group of graduate students on a variety of research projects in the areas of radio-frequency (RF) microelectromechanical systems (MEMS), sensing and power-harvesting applications, as well as RFID sensors for the health monitoring of sensitive equipment. He has been a Principal Investigator (PI) or a co-PI in numerous projects funded by government agencies and industry in these areas. He is currently a key contributor in two DARPA projects at Purdue University focusing on the following: 1) very high quality ($Q > 1000$) RF tunable filters in mobile form factors (DARPA Analog Spectral Processing Program, Phases I, II, and III) and 2) developing comprehensive characterization methods and models for understanding the viscoelasticity/creep phenomena in high-power RF MEMS devices (DARPA M/NEMS S&T Fundamentals Program, Phases I and II). Furthermore, he is leading the experimental program at the Center for the Prediction of Reliability, Integrity, and Survivability of Microsystems funded by the National Nuclear Security Administration. In addition, he is heading the development of the MEMS technology in a U.S. Navy project (Marines) funded under the Technology Insertion Program for Savings program focused on harsh-environment wireless microsensors for the health monitoring of aircraft engines. He has over 130 refereed journal and conference publications in the areas of microwave integrated circuits, sensors, and antennas.

Dr. Peroulis was a recipient of a National Science Foundation CAREER Award in 2008. His students have received numerous student paper awards and other student research-based scholarships. He is a Purdue University Faculty Scholar and was also a recipient of eight teaching awards including the 2010 HKN C. Holmes MacDonald Outstanding Teaching Award and the 2010 Charles B. Murphy Award, which is Purdue University's highest undergraduate teaching honor.

Eric A. Stach received the Ph.D. degree in materials science and engineering from the University of Virginia, Charlottesville.

He was a Staff Scientist and a Principal Investigator with the National Center for Electron Microscopy, Lawrence Berkeley National Laboratory, Berkeley, CA, and as an Associate then a Full Professor with Purdue University, West Lafayette, IN, where he retains an Adjunct appointment. He is currently with the Center for Functional Nanomaterials, Brookhaven National Laboratory, Upton, NY, where he leads the Electron Microscopy Group.

Alejandro Strachan received the B.S and Ph.D. degrees in physics from the University of Buenos Aires, Buenos Aires, Argentina, in 1995 and 1999, respectively.

He is currently an Associate Professor of materials engineering with Purdue University, West Lafayette, IN, and before joining Purdue, he was a Staff Member with the Theoretical Division, Los Alamos National Laboratory, and had postdoctoral and scientist positions with the California Institute of Technology, Pasadena. His research focuses on the development of predictive atomistic and molecular simulation methods to describe materials from first principles with quantified uncertainties and their application to problems of technological importance. Application areas of interest include the following: electronic, thermal, and mechanical properties of nano- and microelectromechanical systems, electronics and energy conversion devices; thermomechanical response of polymer composites and molecular solids; and physics and chemistry of active materials including shape memory and energetic materials.